

DIGITAL TOMOGRAPHIC IMAGING WITH TIME-MODULATED PSEUDORANDOM CODED APERTURE AND ANGER CAMERA

Kenneth F. Koral, W. Leslie Rogers, and Glenn F. Knoll

The University of Michigan, Ann Arbor, Michigan

The properties of a time-modulated pseudorandom coded aperture with digital reconstruction are compared with those of conventional collimators used in gamma-ray imaging. The theory of this coded aperture is given and the signal-to-noise ratio in an element of the reconstructed image is shown to depend on the entire source distribution. Experimental results with a preliminary 4×4 -cm pseudorandom coded aperture and an Anger camera are presented. These results include phantom and human thyroid images and tomographic images of a rat bone scan. The experimental realization of the theoretical advantages of the time-modulated coded aperture gives reason for continuing the clinical implementation and further development of the method.

Application of coded apertures to gamma-ray imaging in nuclear medicine is under active investigation by a number of research groups (1-14). In coded aperture imaging, the conventional pinhole or collimator is replaced by a lead plate with openings arranged in a specific coded pattern. The image is recorded in coded form and must be subsequently decoded. The code is chosen to facilitate this reconstruction process. To date with a few exceptions, most investigators have employed some form of a Fresnel zone plate. Another type of coded aperture in the form of a time-varying hole pattern based on pseudorandom sequences of binary digits was first applied to gamma-ray imaging by Knoll (15,16). Related work including that employing stochastic codes has been reported (17-20). This paper describes the theory of the time-modulated pseudorandom aperture and presents results obtained with an Anger camera.

Coded apertures in general exhibit a number of unique features which make them attractive for

gamma-ray imaging in nuclear medicine. In common with the pinhole and converging-hole collimator they permit magnification of the object so that detector resolution need not limit object resolution. Contrary to the pinhole and converging collimator, however, the field of view is not reduced to a point as magnification is increased but rather approaches the dimensions of the coded aperture as a limit.

Another property peculiar to images formed by coded apertures is their insensitivity to detector non-uniformity and noise. The gains with respect to detector noise or indeed any noise component not modulated by the aperture may be realized because coded apertures can subtend open solid angles that are orders of magnitude greater than conventional apertures. Detector uniformity is of less importance since each point in the source distribution is recorded as coded information over a large region of the detector and nonuniform response is averaged out. These additional degrees of freedom pave the way for innovations in detector design.

We will also show that a coded aperture is capable of giving improved statistical information for a number of nuclear medicine imaging situations. This gain can be thought of as arising from improved utilization of detector area and can be realized for any source region that is more intense than the average taken over the entire field of view. Tomography is an additional feature of coded apertures that results from the fact that each source point is viewed from many angles. Tomographic information is simultaneously obtained for all possible source plane depths without the need to move the detector.

Time modulation of the aperture code yields further advantages over stationary codes such as the conventional Fresnel zone plate. These advantages

Received Oct. 26, 1974; original accepted Dec. 22, 1974.

For reprints contact: Kenneth F. Koral, R 3054 Kresge II University of Michigan Medical Center, Ann Arbor, Mich. 48104.

stem from the fact that the point response function for a stationary code depends on a spatial integral over the recorded data. Both the scale factor and the limits of the integration depend on the source position. For the time-modulated code the point response function depends on a time integration and spatial limits and scale factors do not enter into the problem. This difference manifests itself in the following ways:

1. Source regions focus and defocus smoothly with no coherent artifacts.
2. The source distribution may be reconstructed using a single detector element or widely spaced detectors.
3. The resolution is uniform over the field of view. Radiation incident at other than 90 deg on a zone plate, for instance, is preferentially blocked by the finer rings because of the finite thickness of lead. For the time-modulated plate, the time average distribution of the code over the plate is uniform and this problem is avoided.
4. The mean transmission of the code may be varied as a means for optimizing signal to noise in the image.
5. The time-modulated aperture offers one alternative to the off-axis zone plate and half-tone screen. The off-axis zone plate requires about three times the detector resolution compared with the time-modulated aperture for a given object resolution. This means the Anger camera cannot be used as a detector but one must use instead a film-screen combination with an attendant sacrifice in detection efficiency.

In addition to the advantages offered by time modulation are those that occur simply through digital acquisition and data processing. Among these advantages the following are significant: (A) no film grain noise, (B) increased dynamic range, (C) improved signal to noise in the reconstructed image compared with coherent optical processing, and (D) readily available quantitative results.

In the sections that follow, the theoretical development of a time-modulated aperture for a single detector is outlined and extended to a detector array. Expressions are derived for signal to noise and its dependence on the mean transmission of the code. The performance of a time-modulated aperture and Anger camera-computer combination is illustrated and the results compared with an Anger camera utilizing conventional apertures.

THEORY

The essential features of the time-modulated coded aperture geometry are portrayed in Fig. 1 for a one-

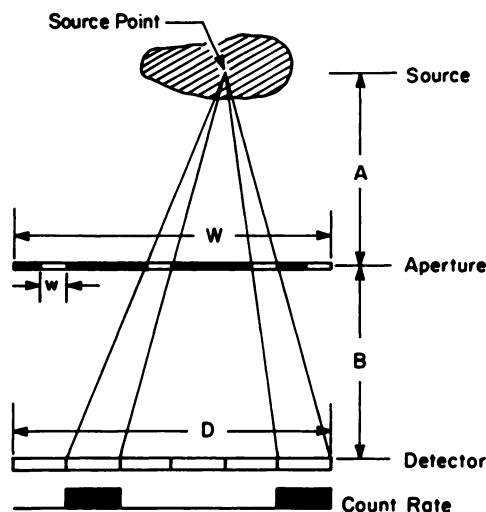


FIG. 1. Geometry in one dimension for time-modulated coded aperture. Counting rate in detector array from one point in source is shown for aperture in permutation depicted.

dimensional aperture and detector. The source-aperture and aperture-detector spacing are represented by A and B, respectively. The aperture is divided into L segments each of width w whose gamma-ray transmittance is 1 or 0. A binary transmittance function is not necessary but yields improved signal to noise over a continuous distribution of transmittance. The detector counting rate due to a single point in the source is shown at the bottom of the figure for the first aperture permutation.

The total measurement time is divided into L equal intervals during which the counts in each detector are recorded. At the end of each interval the code pattern is changed and a new interval is begun. The raw data is composed of the counts in the jth detector during the ν th time interval, $C_{j\nu}$, and the known transmittance of the ith aperture element during the ν th time interval, $T_{i+\nu}$.

Single detector. In Appendix 1 it is shown that the source strength viewed by the jth detector through the ith region of the aperture is given by the correlation coefficient

$$Q_{ij} \equiv \sum_{\nu=1}^L C_{j\nu} T_{i+\nu} - m \sum_{\nu=1}^L C_{j\nu} \quad (1)$$

under the condition that the transmittance fluctuations of different regions of the code pattern are out of phase with each other. In this work, the sequence of code patterns fulfilling this requirement is obtained by cyclically permuting certain pseudorandom binary sequences which are characterized by peaked autocorrelation functions with flat sidelobes (21,22). The constant m in Eq. 1 is the sidelobe-to-peak ratio which is approximately equal to the mean transmission for long code sequences (see Appendix 1).

Figure 2 gives a pictorial rendition of the recon-

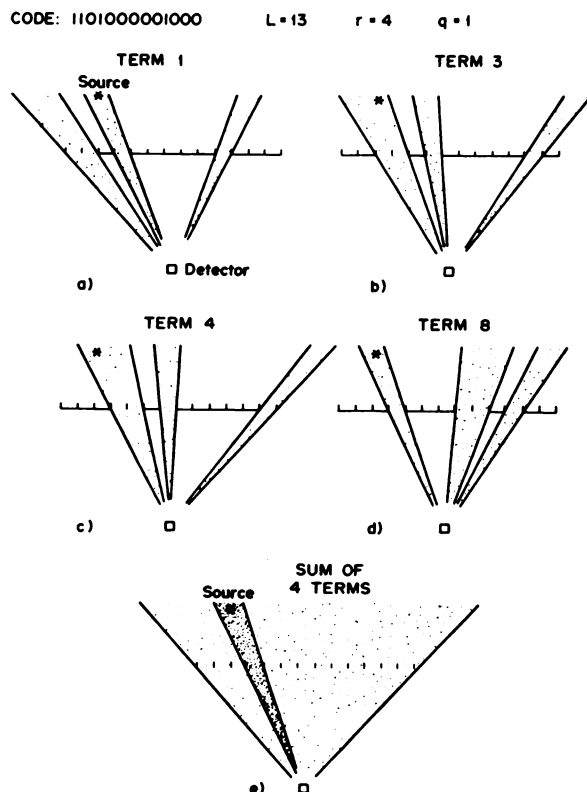


FIG. 2. Typical pseudorandom code is shown at top. Contribution to apparent source strength in each direction is shown by fan-shaped beams in A to D for time intervals 1, 3, 4, and 8. Total image before subtraction of spatially constant term is shown in E, the sum of A to D. Note peak in direction of point source.

struction process spelled out by Eq. 1. The illustrated example is for a single detector, a point source, and a binary sequence of length $L = 13$. For this particular sequence there are four open holes and m has a value of $1/4$. As previously described, counts, C_v , are recorded for each of these 13 cyclic permutations of the code sequence enumerated by $v = 1 \dots 13$. The subscript j is suppressed since only a single detector is considered, and the subscript i , denoting source direction, runs from 0 to $(L - 1)$. Counts will be detected for only those permutations of the code in which an open hole is interposed between the source and detector, namely for $v = 1, 3, 4$, and 8 . For the i directions, the nonzero contributions to the apparent source strengths from the first part of Eq. 1 are shown in Fig. 2A to D. The sum is shown in Fig. 2E. It is seen that, for the sum, the strength is enhanced in the direction of the true source, and all other directions are uniformly covered. A uniform background of the correct size is subtracted from all source strengths through the second part of Eq. 1, leaving a peak in the direction of the source.

For a pseudorandom aperture, the statistical error that accompanies the measurement of source intensity for an element of the image depends on all

source activity within the field of view. This characteristic can be seen qualitatively from Fig. 2 and Eq. 1; the single point source generates a uniform background in the image which can only be subtracted on the average. The statistical noise in this background will add to the uncertainty for all other sources in the field of view. The magnitude of this uncertainty is derived in Appendix 2 where it is shown that for the single detector case, the square of the relative standard deviation, S_i^2 , of the i^{th} source element is given by

$$S_i^2 = \frac{L(r-1)}{r(L-r)} B_i + \frac{L}{r} \frac{1}{N_{i,\text{tot}}} \quad (2)$$

The length of the code sequence is L , r is the number of open holes in the code sequence, and $N_{i,\text{tot}}$ is the total number of counts from the i^{th} source the detector would register through a completely open aperture during the entire measurement. The influence of all the other sources on the measurement of the i^{th} source element is contained in B_i which is the ratio of the total source strength in the field of view excluding the i^{th} source to the strength of the i^{th} source:

$$B_i = \frac{1}{N_{i,j \neq i}} \sum_{j=1}^L N_j \quad (3)$$

Equation 2 holds for codes of arbitrary length, L . For a given code length an optimum value of r may be determined that will minimize the error associated with the measurement of any specific source region (i.e., for any given value of B_i).

Table 1 gives some values for the optimum transmission, $T \equiv r_{\text{opt}}/L$, obtained by evaluating the expression for r_{opt} in Appendix 2 for some limiting values of B_i . For the case of a uniform field flood, $B_i = L - 1$, the optimum T is $1/L$. This means that the optimum code would contain only a single open element. As the code is cyclically permuted, the single open element traverses the aperture and the optimum coded aperture is nothing more than a scanning pinhole. When $B_i = 0$, corresponding to an

TABLE 1. OPTIMUM CODE TRANSMISSION FOR EXTREME SOURCE DISTRIBUTIONS

Ratio of sum of all other source strengths over i^{th} source strength, B_i	Optimum number of open elements, r	Optimum transmission, $T \equiv r_{\text{opt}}/L$
0	L	1
1	$(L-1)/2$	$\approx 1/2$
$L-1^*$	1	$1/L$

* L , code length.

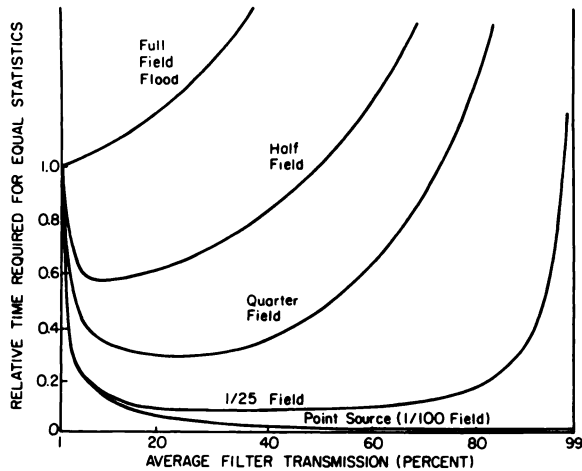


FIG. 3. Relative imaging time required to obtain given statistical accuracy for intensity in uniformly filled regions of field. Correct choice of mean transmission of code results in minimizing imaging time for indicated source distributions. Five cases ranging from full field flood to point source are shown.

isolated point source, the optimum \bar{T} is 1, meaning that best statistical information is obtained by merely counting the point source. If its position is to be determined, at least one element must remain closed and the optimum aperture is a scanning point absorber (i.e., an inverse pinhole). When B_i is greater than $(L - 1)$, signifying that the i th source is weaker than the average of all other sources, an optimum cannot be found for physical values of \bar{T} . Under these conditions, minimum error is obtained with the scanning pinhole.

Additional insight into the efficiency question can be obtained by examining the case of a distribution of uniformly intense sources filling various fractions of the field of view of the single detector element. The unfilled fraction contains no activity. If the relative imaging time required to obtain a given statistical accuracy for the intensity of the filled fraction of the field is plotted as a function of the average code transmission, \bar{T} , the nature of the optimum in \bar{T} is clarified. Figure 3 shows such a plot for various filled fractions of the field of view and an assumed code length of 100 elements. As discussed previously, for a full field flood, the best that can be done is $\bar{T} = 1\%$ which is the case of the scanning pinhole. If half the resolution elements are filled, a 40% reduction in time can be achieved with an average transmission of 10%. The curves are characterized by a rather broad minimum and near optimum conditions can be obtained for the illustrated cases by selecting codes with $\bar{T} = \sqrt{L}$, or 10% in this instance. Such a choice adds only 5% to the imaging time for the full field flood. It must be pointed out, however, that the measurement of zero activity in the cold fraction of the field is made with reduced statistical accuracy so

the coded aperture offers advantages only in the measurement of sources more intense than the mean. In many instances, however, parts of the cold region lie far from the source distribution of interest. Thus a priori information concerning the source permits one to ignore these regions of increased noise.

A straightforward geometric argument gives the transverse resolution for the coded aperture in the limit of infinite detector resolution as

$$R = \left(1 + \frac{A}{B}\right)w \quad (4)$$

where w is the width of an aperture element. This resolution is the same as that for a pinhole of diameter w . The actual resolution is sensitive to the specific method used to back-project the correlation strength. Also to Eq. 4 must be added the effect of detector resolution, R_1 yielding

$$R_t^2 = R^2 + \left(\frac{A}{B} R_1\right)^2 \quad (5)$$

if the two contributions are assumed to add in quadrature. As with a pinhole the contribution from detector resolution becomes small for $A \ll B$.

Monte Carlo computer simulations for simple geometric cases were carried out and confirmed the predictions of the theoretical model (15). Resolution was shown to be that of a pinhole with diameter equal to the aperture-element diameter and general trends in the statistical noise as a function of the transmittance of the code were demonstrated to be as previously described.

Multielement detectors. Extension of the discussion to multielement detectors such as the Anger camera is facilitated by the fact that the information in the various detector resolution elements is independent. The composite image may be considered as a linear sum of properly scaled and shifted images from each of these detector elements.

The total field of view for the coded aperture and multielement detector is composed of all the individual fields of view and is illustrated in the upper left of Fig. 4. For comparison, the fields of view for the pinhole, parallel-hole, and converging collimators are also shown. One sees that the coded aperture has a significantly larger field of view than the pinhole for small source-to-aperture distances and a larger field of view than any of the collimators for large distances.

Neglecting solid angle, the coded aperture sensitivity is uniform across the field of view until the detector begins to be obscured by the edge of the aperture. At this point the sensitivity starts decreasing in direct proportion to the decrease in effective detector area. For a square detector and aperture the

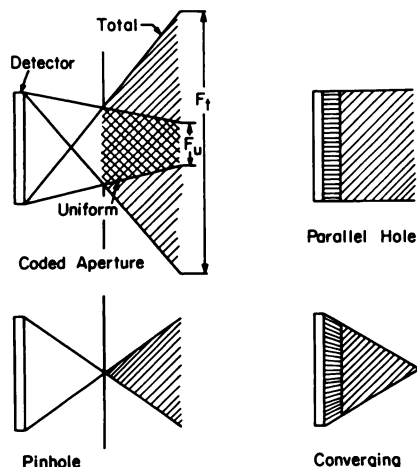


FIG. 4. Comparison of field of view for coded aperture, pinhole, parallel-hole, and converging collimators. For coded aperture, there is reduced field of view over which sensitivity is uniform. Total field for coded aperture is larger than that of any of other systems.

uniform field is also a square. The width of the square is F_u^* and is given by:

$$F_u = \left(1 + \frac{A}{B}\right)W - \frac{A}{B}D. \quad (6)$$

W is the length of a side of the aperture and D is the length of a side of the detector. A and B are the source-aperture and aperture-detector distance as before. The total field of view for the same geometry is a square of width F_t where

$$F_t = \left(1 + \frac{A}{B}\right)W + \frac{A}{B}D. \quad (7)$$

In most practical situations, the variation of open solid angle across the field of view modifies the uniformity of response. This is particularly true when the aperture plate has thickness approaching or exceeding the diameter of the individual holes. This problem assumes additional importance when one attempts to place the source as close as possible to the plate in order to achieve improved counting rates and resolution. Figure 5 shows plots of response calculated for a pinhole and for the 4×4 -cm experimental aperture described later. The responses are normalized to 100% and are shown for a source plane with $A = 1$ and 3 cm assuming a plate thickness of 2 mm. The uniformity is improved in both cases and much improved with the smaller A for the coded aperture compared with the pinhole.

* If W is smaller than D , there is a distance, A_v , at which $F_u = 0$. At distances larger than A_v , in this case, the signs of the two terms in Eq. 6 must be reversed. This reflects a transition from a detector-limited to aperture-limited imaging system.

Since the resultant image is a linear superposition of statistically independent images from each of the participating detectors, the noise will combine in quadrature sum. The noise in each of the component images depends on the source distribution in the field of view of each of the detector elements. However, the number of detectors contributing to the reconstruction of the image element decreases for elements near the edge of the field. Therefore, as one approaches the edge of the field of view the signal to noise in general deteriorates compared with the signal to noise in the region of uniform field of view.

When there are many detector elements, the pseudorandom coded aperture has tomographic capabilities. This tomography is demonstrated for a point source in Fig. 6. The correlation strengths projected back have the uniform background subtracted so each detector projects a fan-shaped beam only in the direction of the source. The contributions from

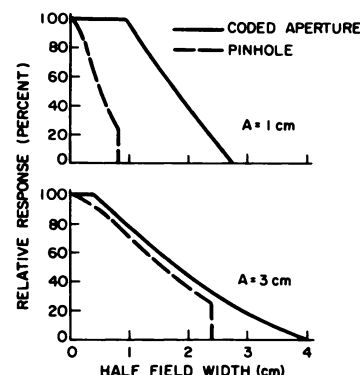


FIG. 5. Comparison of calculated relative field uniformity across center of field for 3.6-mm diam pinhole and 4×4 -cm coded aperture with 3.6-mm diam elements. Calculation was done for untapered holes in 2-mm thick lead assuming no penetration. Sharp cutoff in pinhole corresponds to edge of detector. Uniformity of coded aperture response is limited by small size of experimental aperture. $B = 15.7$ cm.

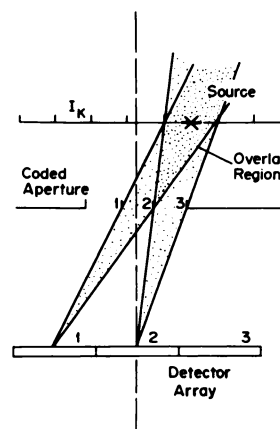


FIG. 6. When multielement detector is used with coded aperture, tomographic reconstruction is possible as illustrated for point source. Strongest peak occurs at actual depth of source.

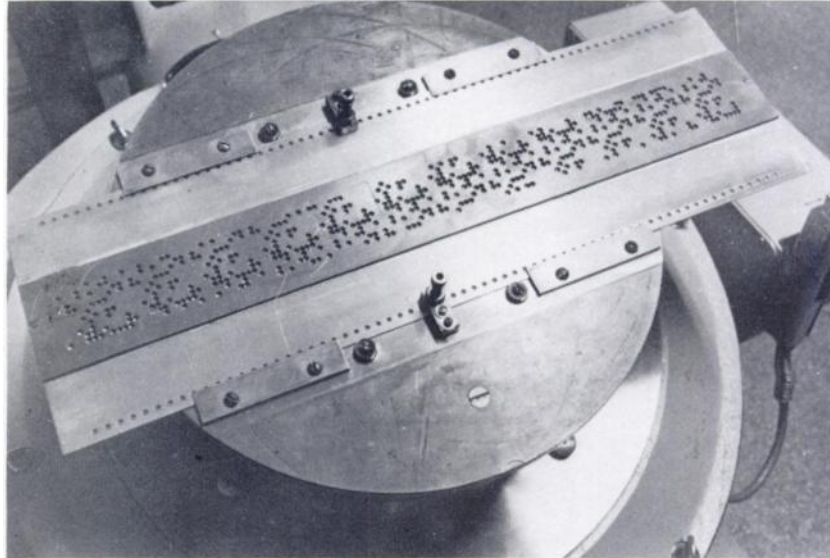


FIG. 7. Photograph of coded lead plate used to obtain results in this paper. Plate slides to provide time modulation of code pattern as illustrated in Fig. 8.

each detector coincide at the depth of the source and defocus at other depths.

The shape of the point spread function in the longitudinal direction is complex and obviously depends on the shape chosen for the back-projected beam and the angle subtended by the aperture and detector. The depth of field on axis for perfect camera resolution is given approximately by:*

$$D_t = 2 \frac{(A + B)}{D} R \quad (8)$$

where R is the lateral resolution and D is the detector diameter. A change in depth of $D_t/2$ on either side of the focal plane will double the apparent width of a point source if $D_t \ll A$. The depth of field is reduced as the aperture-to-source distance, A , decreases, or the detector diameter increases, since the source element is looked at from a larger range of angles. The effects of finite plate thickness and solid angle are not included.

Figure 6 also illustrates a problem encountered in the tomographic response of this system. As the point source defocuses, the centroid of information responsible for the image follows a path that intersects either the center of the aperture or the center of the detector region that views the source. This causes an apparent shift in the size and position of sources as they are defocused. It turns out that if the total field F_t is imaged over the same number of elements for each depth, the location of a feature in the $3 - D$ source will not change with depth. This method does require that the calibration (mm/image element) changes between tomograms. The actual length of

in-focus features can still be measured, however, by the use of the calibration appropriate for the given depth.

EXPERIMENTAL RESULTS

Gamma-ray images have been obtained with the prototype time-modulated aperture pictured in Fig. 7 using an Anger camera detector. The lead code plate is 2 mm thick and holes are 3.6 mm in diameter. The binary sequence on the illustrated plate is 121 elements long with 40 open holes, giving values of 40 and 13 for r and q , respectively. The sequence is repeated 11 times in the 11 rows. Each row, however, has the sequence cyclically shifted 11 elements from the preceding row. A 3.9-cm square aperture beneath the code plate defines an 11×11 area. As the code plate is translated, each of the 121 regions describes the entire binary sequence with a phase that differs from all of the other regions. This property is more clearly illustrated in Fig. 8 which shows three successive frames for a hypothetical 9-element code plate.

Data acquisition and processing are accomplished with an MDS data collection system based on a NOVA 1200 series computer. Each of the 121 64×64 element data frames is written sequentially on a disk for poststudy processing. Image reconstruction is performed in two steps.

In the first step, the matrix of correlation coefficients is calculated:

$$Q_{ij} = \sum_{v=1}^{121} C_{vj} (T_{i+v} - m) \quad (9)$$

where Q_{ij} is the correlation of the j^{th} detector with the i^{th} aperture and C_{vj} is the detected counts for the j^{th} detector in the v^{th} time interval. An inscribed

* Again, for distances greater than A_v , $2(A + B)/D$ change to $2A/W$.

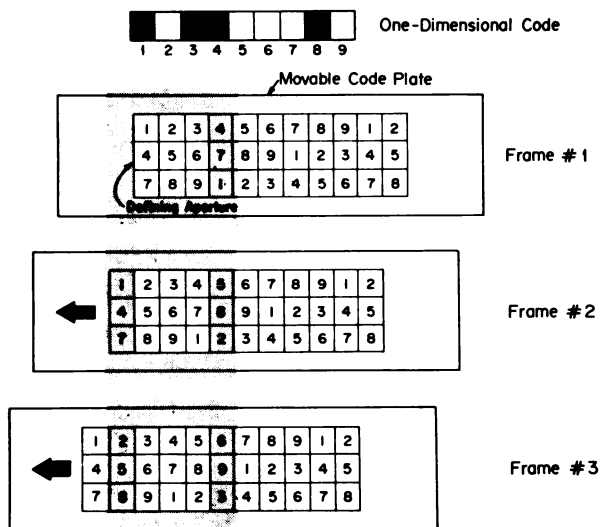


FIG. 8. Hypothetical 9-element code and code plate constructed from it. Lead defining aperture selects various 3×3 -element patterns as plate is indexed to left. First three out of nine frames or time intervals are shown. Note that all positions inside aperture follow through code in order, but out of phase with all other positions (e.g., lower right: 9, 1, 2 . . .).

square in the circular detector field is digitized into a 46×46 -element array so the subscript j assumes values 1 through 2,116. The subscript i ranges from 0 to 120 and enumerates the different aperture regions. Calculation of the 256,036 elements in the correlation matrix Q takes 10 min. These elements are calculated in blocks of 5,566 and stored on disk.

In the second step, a tomographic slice of the image is formed from a linear combination of the previously calculated correlation coefficients:

$$I_k = \sum_{i,j} \alpha_{ijk} Q_{ij} \quad (10)$$

where I_k is the intensity of the k^{th} image element. The coefficients α_{ijk} have values between 0 and 1 and serve to select only those aperture-detector pairs that contribute to the k^{th} image element. For example, in Fig. 6, for the image element containing the source, only $Q_{2,1}$ and $Q_{3,2}$ would be combined. In general, most α 's are 0; nonzero values less than 1 can provide for interpolation of a given Q among several image elements. The summation over j expresses the superposition of the appropriately shifted and scaled images from the 2,116 different detectors. The process requires 10 min of computing time for each tomographic slice.

In most of the images that follow, the coded aperture image is compared with a stationary pinhole image taken with identical source-aperture-detector spacing. The pinhole employed is simply one of the holes in the code plate with all of the others being blocked. This insures comparison at equal theoretical resolution. It should also be pointed out that the pin-

hole images use the full detector area while the coded aperture images are reconstructed with only $2/\pi$ of the detector area because of limitations in computer core memory size.

Figure 9 compares the image quality of the coded aperture with the pinhole in the case of good counting statistics and under the conditions that the object is well within the field of view for both apertures. The photographs were taken under identical conditions of intensity and contrast and there was no background subtraction. The coded aperture image accurately reproduces the intensity profile but shows decreased resolution and some slight structure compared with the pinhole image. This departure from the result predicted by simple theory is probably caused by several factors including lack of interpolation in the reconstruction algorithm and spatial distortion in the Anger camera. The relative importance of these effects has not yet been determined. The coded aperture image has been corrected for field nonuniformity since different source regions are viewed by different numbers of detector elements.

Figure 10 compares the pinhole and coded apertures for the case of poor counting statistics. The thyroid phantom was filled with $23 \mu\text{Ci}$ of $^{99\text{m}}\text{Tc}$ and positioned 9.3 cm from the aperture which was in turn 16.4 cm from the detector. Imaging time was 120 sec in each case. Although both images are very noisy, the coded aperture image demonstrates better signal to noise than the pinhole image. A quantitative estimate of this improvement is indicated below the images where the mean and relative standard deviation over small regions are shown. The mean for the hot and cold spot differs from 1.0 and 0, respectively, because of finite resolution. The values shown are sensitive to the location and size of the regions and so are subject to some error. Care was taken to keep the images to the same scale and to avoid any smoothing so that the comparison between the pinhole and coded aperture was fair. Improve-

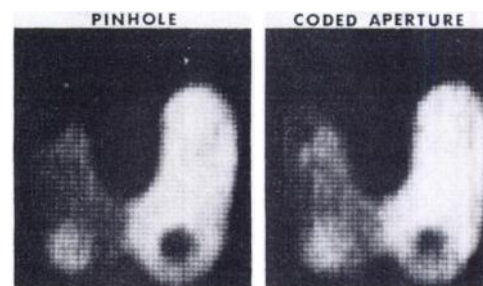


FIG. 9. Comparison of coded aperture to pinhole for good counting statistics with Picker thyroid phantom. Source: 1 mCi $^{99\text{m}}\text{Tc}$, time: 6 min, $A = 9.9$ cm, and $B = 22$ cm. Coded aperture shows slight reduction in resolution and beginnings of unwanted structure resulting in part from lack of interpolation in reconstruction algorithm.

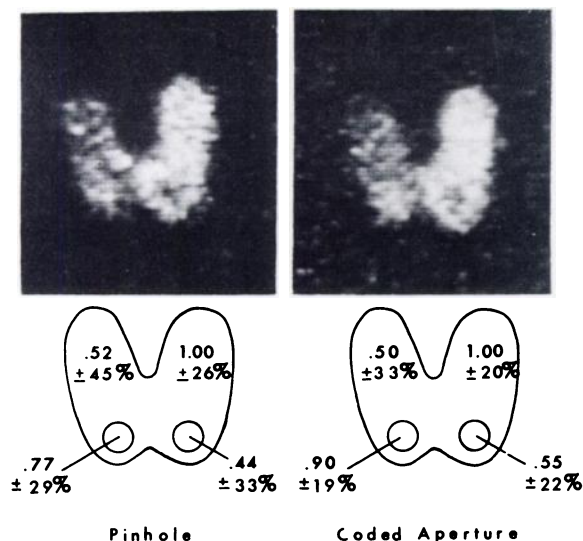


FIG. 10. Comparison of coded aperture to pinhole for poor counting statistics. Both images are noisy but coded aperture image displays more uniformity. Below, intensity and relative standard deviation are shown for small regions in image. Although these values depend somewhat on region location, they consistently show higher signal to noise with coded aperture.

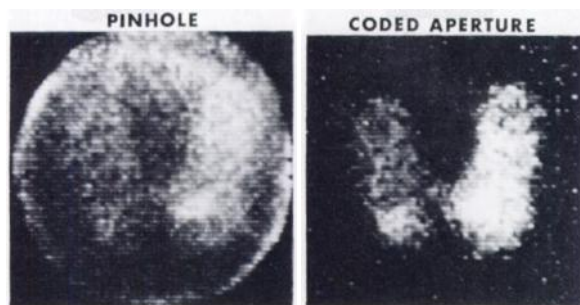


FIG. 11. Comparison of coded aperture to pinhole with simulated detector noise. A = 9.9 cm and B = 22 cm. Advantage of coded aperture in this situation is dramatic. Hot region on right lobe of phantom is external contamination.

ment over the entire image is consistent with the fact that the image strength, even in the low activity areas shown, is higher than the average in the total field of view. The coded aperture image displays increased noise in the image field surrounding the phantom where the image strength is below the mean.

Comparison of the pinhole and coded aperture performance in the case of noise unmodulated by the aperture is shown in Fig. 11. Here the 100- μ Ci thyroid phantom is imaged for 2 min in the presence of a second source located between the aperture and the detector. This noise source simulates detector noise, background from poor shielding, or even gamma rays which penetrate the aperture plate. The noise counting rate in this case was 45,000 cpm compared with a signal rate of 10,200 cpm for the pinhole. The coded aperture signal rate was about 20,000 cpm.

The pinhole image in Fig. 11 is barely discernible

above the background while the coded aperture image is only slightly degraded. No background subtraction is employed in these images and the hot region on the right lobe is surface contamination of the phantom. The noise immunity demonstrated in these images shows that good images may be obtained in spite of detector noise and that considerable penetration of the aperture plate can be tolerated. The importance of the latter is that relatively thin plates with small diameter holes can be utilized to obtain good image resolution for the higher-energy isotopes.

As previously discussed, the coded aperture gives tomographic images when many detector elements are employed. Examples of the tomographic response are shown in Fig. 12. Two-centimeter high numerals made from capillary tubing were filled with ^{99m}Tc and positioned 1, 2, and 3 cm from the aperture plate which was in turn 21 cm from the detector face. Again, the pinhole image is given for reference. There is no background subtraction. In addition to demonstrating tomography with smooth defocusing, this picture also shows the preservation of the size of the object and illustrates the increased field of view for the coded aperture especially when the desire for high resolution dictates small ratios of A/B. In this case the "2" is almost entirely missing from the pinhole picture yet is imaged in its entirety by the coded aperture.

Some of these same features are again illustrated in Fig. 13 which shows two tomographic bone images of a young rat taken with the coded aperture and compares them with the equivalent pinhole and with

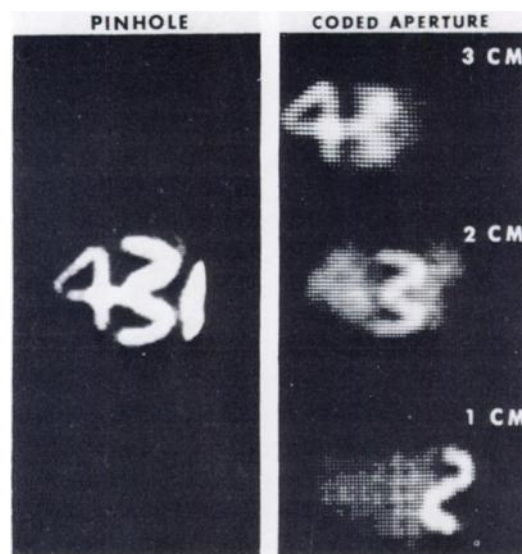


FIG. 12. Illustration of tomography with coded aperture. Three numerals, situated at depths differing by 1 cm, appear in focus when image is reconstructed at their respective depths. In other planes they are smoothly defocused. Note also difference in field of view for coded aperture.

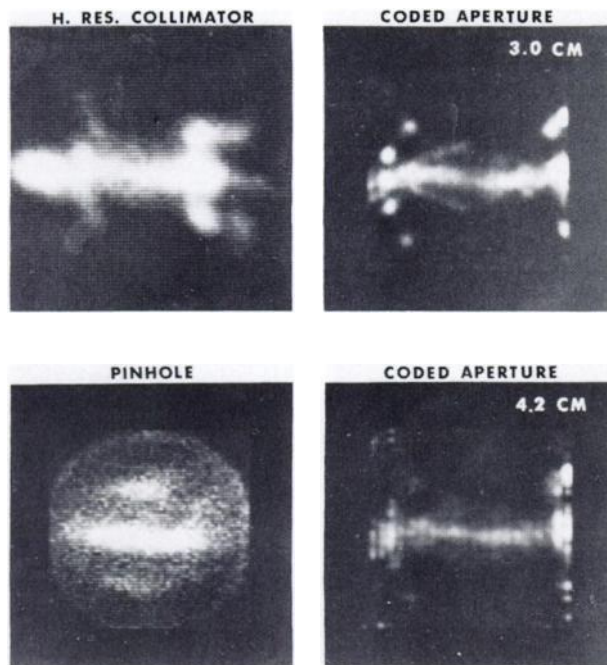


FIG. 13. Comparison of coded aperture with pinhole and high-resolution parallel-hole collimator in case of rat bone scan. Imaging time was 5 min for each system. Pinhole image would be somewhat improved with solid-angle correction, although this correction is different for different depths. Good tomographic resolution of rib cage outline and other features is shown with coded aperture.

the Searle Radiographics high-resolution parallel-hole collimator. Imaging was done $2\frac{3}{4}$ hr after administering $150 \mu\text{Ci}$ of $^{99\text{m}}\text{Tc}$ -labeled diphosphonate. For both the pinhole and coded aperture images the ventral surface of the rat was 2 cm from the aperture, and the aperture-detector distance was 15.7 cm. The rat was positioned at the face of the high-resolution collimator. In each instance the imaging time was 5 min. In these images no background subtraction was employed but the bladder activity was permitted to saturate the film in order to bring out the lower activity regions of the image. The 8-cm field of view in the tomogram for $A = 3$ cm extends from the base of the skull to the bladder. The shoulder and elbow joints in the forelegs are well visualized and the heads of the right tibia and femur are resolved. The rib cage is distinct and there is a hint of the kidneys. At 4.2 cm the vertebral column is more sharply defined and the other structure is blurred. Some structure appears in this image which again arises from lack of interpolation in the reconstruction program. The image from the high-resolution collimator provides a greater field of view but does not have equivalent resolution while the pinhole image resolves part of the rib cage outline from the vertebral column but has a much reduced field of view.

The coded aperture has also been used for human thyroid imaging with pertechnetate. An example is

given in Fig. 14 where a 6-min image of a normal thyroid with $A = 6.4$ cm is shown. The image taken with an equivalent pinhole was similar as tomographic effects were not great in this case. The tomography should be improved upon construction of a smaller plate holder which will allow placement of the neck adjacent to the plate. It is hoped that the coded aperture will be particularly effective in the case of patients suspected of having small hot nodules. The present plate would be used with either the standard dose of $^{99\text{m}}\text{Tc}$ or perhaps with ^{125}I .

DISCUSSION

We have attempted to describe the basic theory of a time-modulated coded aperture and to illustrate some of its imaging characteristics as compared, in most cases, with a stationary pinhole. The pinhole was used for comparison because it has a similar dependence of resolution on geometry and because it was experimentally convenient. Other apertures may be indirectly compared by the pinhole. Features such as magnification, increased field of view, and tomography are offered by conventional collimators or apertures but not all at once. Efficiency optimization and insensitivity to detector noise and to detector nonuniformity are characteristics restricted to coded apertures. The advantages are not obtained without accompanying disadvantages, however, and the ultimate fate of coded aperture imaging in nuclear medicine depends on the extent to which the disadvantages can be minimized and the advantages exploited.

Considerable early interest in coded apertures was generated by the ability to use a much greater fraction of gamma rays to form the image and the potential for reducing statistical noise as a result. We have shown that, for the methods outlined here, a gain in statistical accuracy is only obtained for source regions more intense than the source intensity averaged over the full field of view. Furthermore, this gain is realized at the expense of added noise in source regions below the mean. When these regions lie mainly outside the region of interest, then a net gain is realized.



FIG. 14. Coded aperture image (6 min) of normal thyroid in human patient. $A = 6.44$ cm, $B = 22.3$ cm, and dose = $2 \text{ mCi } ^{99\text{m}}\text{Tc}$ pertechnetate.

In a sense, this gain stems from the fact that we have a priori knowledge about the source distribution that allows us to ignore this noise. It is clear that the best gains in statistical precision will be realized when imaging small hot objects in relatively cold backgrounds. However, large diffuse source distributions may also be recorded with approximately the same statistical error as with conventional techniques.

From a practical standpoint, problems arise because of the need to decode the image. These are predominantly cost- and time-related problems with engineering solutions. For example, the small size of the aperture used in these experiments, which limited the field of view at interesting resolutions, was determined largely by the desire to perform the data processing on an existing clinical minicomputer. It should certainly be possible to employ improved reconstruction algorithms in combination with available hardwired accessories to generate images in close to realtime with an attendant reduction in data storage requirements. Alternative codes and various analog reconstruction schemes are also amenable to fast decoding so that it is likely that image reconstruction will not prove to be a fundamental problem.

More work is needed to implement fast decoding and to solve some of the difficulties encountered in filling the image array. At the present time a number of special purpose apertures are under construction that will permit evaluation of the technique for solving specific human and animal imaging problems. We are optimistic that some form of coded aperture imaging will be found clinically useful and usable.

APPENDIX 1. RECONSTRUCTION BY CORRELATION—SINGLE DETECTOR

Consider the geometry of Fig. 1. We wish to show that for an appropriate sequence of code patterns it is possible to reconstruct the projected source distribution with the information recorded by one of the illustrated detector elements. The total measurement time is divided into L intervals enumerated by the subscript ν ; $\nu = 1 \dots L$. Define the following:

$N_{i\nu} \equiv$ The number of gamma rays emitted per unit solid angle from the i^{th} source element in the ν^{th} time interval.

$T_{i+\nu} \equiv$ The gamma-ray transmission of the i^{th} aperture element during the ν^{th} time interval. We will be considering sequences of 1's and 0's that will be cyclically permuted by one step for each time interval. The i^{th} aperture element will therefore trace out this transmission sequence as a function of ν .

$C_{i\nu} \equiv$ The number of photons detected that pass through the i^{th} aperture element during the ν^{th} time interval assuming a

unit solid angle detector. Note for the single detector case that the i^{th} aperture element defines only one region in the source so that the single subscript i may be used unambiguously for both source and aperture elements.

Also:

$N_i^{\text{tot}} \equiv \sum_{\nu=1}^L N_{i\nu}$, the total number of gamma rays emitted by the i^{th} source per unit solid angle during the entire measurement.

$\bar{N}_i \equiv \frac{N_i^{\text{tot}}}{L}$, the average number of gamma rays emitted by the i^{th} source per time interval.

$C_\nu \equiv \sum_{i=1}^L C_{i\nu}$, the number of gamma rays detected from all sources during the ν^{th} time interval.

$C^{\text{tot}} \equiv \sum_{\nu=1}^L C_\nu$, the total number of gamma rays detected over all intervals.

We note that counts detected from the i^{th} source are equal to the number emitted per unit solid angle times the aperture element transmission,

$$C_{i\nu} = N_{i\nu} T_{i+\nu}. \quad (1-1)$$

We have, as yet, said nothing concerning the requirements to be placed on the aperture transmission as a function of position and time, $T_{i+\nu}$. We will show that it is sufficient to employ a binary sequence of length L that is characterized by a peaked cyclic autocorrelation function with flat wings or sidelobes. This property is written

$$\Phi_\delta = \sum_{i=1}^L T_i T_{i+\delta} = \begin{cases} r & \text{if } \delta = 0, L, 2L, \dots \\ q & \text{for all other } \delta \end{cases} \quad (1-2)$$

where the subscripts on T are evaluated modulo L . The peak height of the autocorrelation is r and the height of the sidelobe is q . The peak height is seen to be equal to the number of 1's in the sequence and is related to q and L by

$$q/r = \frac{r-1}{L-1} = m. \quad (1-3)$$

The ratio, m , is seen to approach the average transmission, $T \equiv r/L$ for r and $L \gg 1$.

We first evaluate the correlation between the detected counts and the k^{th} aperture transmittance;

$$P_k = \sum_{\nu=1}^L C_\nu T_{\nu+k} \quad (1-4)$$

and from 1-1 and the definition of C_ν

$$P_k = \sum_{\nu=1}^L \sum_{i=1}^L N_{i\nu} T_{i+\nu} T_{\nu+k}. \quad (1-5)$$

Dividing the sum into $i = k$ and $i \neq k$ parts and reversing the order of summation yields

$$P_k = \sum_{i \neq k}^L \sum_{\nu=1}^L N_{i\nu} T_{i+\nu} T_{\nu+k} + \sum_{\nu=1}^L N_{k\nu} T_{k+\nu} T_{\nu+k}. \quad (1-6)$$

Replacing $N_{i\nu}$ and $N_{k\nu}$ by their average values, summing over ν , and using Eq. 1-2 gives:

$$P_k = q \sum_{i \neq k}^L \bar{N}_i + r \bar{N}_k. \quad (1-7)$$

We now define

$$\begin{aligned} Q_k &\equiv P_k - q \sum_{i=1}^L \bar{N}_i \\ Q_k &= q \sum_{i \neq k}^L \bar{N}_i + r \bar{N}_k - q \sum_{i=1}^L \bar{N}_i \\ Q_k &= (r - q) \bar{N}_k. \end{aligned} \quad (1-8)$$

Thus we see that Q_k is proportional to the average source strength, N_k , which is the desired result. The term which was subtracted from P_k to obtain this result,

$$q \sum_{i=1}^L \bar{N}_i = q \frac{\bar{C}}{\bar{T}} = q \frac{C^{\text{tot}}/L}{r/L} = m \sum_{\nu=1}^L C_\nu \quad (1-9)$$

is seen to be a constant average background directly proportional to the mean counting rate per time interval from all sources, \bar{C} , and inversely proportional to the mean transmission of the code sequence, \bar{T} .

APPENDIX 2. SIGNAL-TO-NOISE RATIO— SINGLE DETECTOR

We have shown in Appendix 1 that Q_k is proportional to the source strength in the case of a single detector. In the multidetector development the proportionality constant was dropped as unnecessary. Here, we solve explicitly for the strength estimate and then develop an equation for the error in that strength estimate. Finally, we minimize the error with respect to the mean transmittance of the code T .

From (1-8) we solve for the strength estimate of the k^{th} source element:

$$\bar{N}_k = \frac{1}{(r - q)} Q_k \quad (2-1)$$

or

$$\bar{N}_k = \frac{1}{(r - q)} \sum_{\nu=1}^L C_\nu \left[T_{\nu+k} - \frac{q}{r} \right].$$

Now define

σ_k^2 = The variance in the k^{th} source strength, \bar{N}_k .

σ_ν^2 = The variance in the number of counts during the ν^{th} time interval, C_ν .

If we assume that the statistical error of each count C_ν is independent, we may evaluate the expected variance in N_k as:

$$\sigma_k^2 = \frac{1}{(r - q)^2} \sum_{\nu=1}^L \left(T_{\nu+k} - \frac{q}{r} \right)^2 \sigma_\nu^2. \quad (2-2)$$

But since each recorded count C_ν is a Poisson variable:

$$\sigma_\nu^2 = C_\nu \quad (2-3)$$

Using (2-3) and the fact that $T_{\nu+k}^2 = T_{\nu+k}$:

$$\begin{aligned} \sigma_k^2 &= \frac{1}{(r - q)^2} \left[\sum_{\nu=1}^L \left(1 - \frac{2q}{r} \right) T_{\nu+k} C_\nu + \left(\frac{q}{r} \right)^2 \sum_{\nu=1}^L C_\nu \right] \\ &= \frac{1}{(r - q)^2} \left[\left(1 - \frac{2q}{r} \right) P_k + \left(\frac{q}{r} \right)^2 C^{\text{tot}} \right]. \end{aligned}$$

Substituting:

$$P_k = q \sum_{\nu \neq k}^L \bar{N}_\nu + r \bar{N}_k$$

$$C^{\text{tot}} = r \sum_{\nu=1}^L \bar{N}_\nu$$

and combining sums gives the variance of the k^{th} source strength:

$$\sigma_k^2 = \frac{q}{(r - q)r} \sum_{\nu=1}^L \bar{N}_\nu + \frac{r - 2q}{r(r - q)} \bar{N}_k. \quad (2-4)$$

The square of the relative standard deviation of the k^{th} source strength is:

$$S_k^2 \equiv \frac{\sigma_k^2}{(\bar{N}_k)^2}.$$

Therefore,

$$S_k^2 = \left[\frac{q}{r(r - q)} \sum_{\nu=1}^L \frac{\bar{N}_\nu}{\bar{N}_k} + \frac{r - 2q}{r(r - q)} \right] \frac{1}{\bar{N}_k}.$$

If we further substitute:

$$B_k \equiv \sum_{\nu \neq k}^L \frac{N_\nu}{\bar{N}_k}$$

$$N_k^{\text{tot}} = L \bar{N}_k$$

$$q = \frac{r(r - 1)}{L - 1}$$

Then,

$$S_k^2 = \left[\frac{L(r-1)}{r(L-r)} B_k + \frac{L}{r} \right] \frac{1}{N_{k \text{ tot}}} \quad (2-5)$$

This is the expression for the relative standard deviation of the k^{th} source strength that we sought.

Choosing an optimum for the average transmittance \bar{T} involves minimizing the error given in Eq. (2-5) with respect to r . This optimum will, in general, differ for various source regions through the influence of the source-strength-ratio term B_i . The result is:

$$(r_{\text{opt}})_i = \frac{L - B_i}{B_i - 1} \left[\left(\frac{B_i(L-1)}{L - B_i} \right)^{1/2} - 1 \right]. \quad (2-6)$$

Even though a variable \bar{T} across the aperture is implied by this source-dependent optimization, a constant value equal to

$$\bar{T} = \frac{1}{\sqrt{L}}$$

will yield near minimum error for nearly all source distributions where no single source element dominates the total.

ACKNOWLEDGMENTS

This work has been carried out with the support of NiH Grant GM16188, Nuclear Medicine Research Fund, the Michigan Memorial Phoenix Project, and NCI Fellowship 1 F22 CA-0612-01. The authors wish to acknowledge the many contributions of A. Z. Akcasu and R. S. May who pioneered the theoretical development of time-modulated apertures for gamma-ray imaging and also the continuing enthusiastic encouragement of W. H. Beierwaltes in the pursuit of high-resolution imaging.

REFERENCES

1. BARRETT HH: Fresnel zone plate imaging in nuclear medicine. *J Nucl Med* 13: 382-385, 1972
2. BARRETT HH, HARRIGAN FA: Fresnel zone plate imaging of gamma-rays; theory. *Appl Optics* 12: 2686, 1973
3. CHANG LT, KAPLAN S, MACDONALD B, et al: A method of tomographic imaging using a multiple pinhole coded aperture. *J Nucl Med* 15: 1063-1065, 1974
4. DICKE RH: Scatter-hole cameras for x-rays and gamma-rays. *Astrophys J* 153: L101, 1968
5. FARMELANT MH: Improved anatomical definition by a Fresnel zone plate imager. *J Nucl Med* 14: 393-394, 1973
6. HAYAT GS: *X-ray and γ -ray Imaging with Multiple Pinhole Cameras*, Ph.D. thesis, State University of New York, Stony Brook, 1971 (University Microfilm #72-98498)
7. JASZCZAK RJ, MOORE FE, WHITEHEAD FR: Use of an array of three off-axis zone plates for large field of view gamma-ray imaging. In *Proceedings of the SPIE Seminar on Application of Optical Instrumentation in Medicine II*, Chicago, Ill, November 1973
8. MACDONALD B, CHANG LT, PEREZ-MENDEZ V, et al: Gamma-ray imaging using a Fresnel zone plate aperture, multiwire proportional chamber detector and computer reconstruction. *IEEE Trans Nucl Sci* 21: 678-684, 1974; Lawrence Berkeley Laboratory Report #LBL2048, November 1973
9. MACOVSKI A: Gamma-ray imaging system using modulated apertures. *Phys Med Biol* 19: 523, 1974
10. LINDGREN AG, GUHA OK, SPENCE JE: A noise analysis of Fresnel zone plate imaging systems. In *Digest of Papers, 1974 International Optical Computing Conference*, April 9-11, 1974, Zurich, Switzerland, IEEE Catalog #CH0862-3C
11. PALMIERI TM: *The Multiplexed Pinhole Camera*. Livermore, Calif, University of California Preprint #UCRL-75506
12. ROGERS WL, HAN KS, JONES LW, et al: Application of a Fresnel zone plate to gamma-ray imaging. *J Nucl Med* 13: 612-615, 1972
13. TIPTON MD, DOWDY JE, BONTE FJ, et al: Coded aperture imaging using on-axis Fresnel zone plates. *Radiology* 112: 155, 1974
14. WALTON PW: An aperture imaging system with instant decoding and tomographic capabilities. *J Nucl Med* 14: 861-863, 1973
15. KNOLL GF: Photon imaging using statistical filters. SRC Research Grant B/RG/3192 Final Report, Science Research Council, London, May 15, 1973
16. KNOLL GF, MAY RS, AKCASU Z: Pseudorandom filters and correlation analysis applied to gamma ray imaging. *J Nucl Med* 15: 507, 1974
17. AKCASU AZ, MAY RS, KNOLL GF, et al: Coded aperture gamma-ray imaging with stochastic apertures. In *Proceedings of the SPIE Seminar on Application of Optical Instrumentation in Medicine II*, Chicago, Ill, November 1973, and *Opt Eng* 13: 117, 1974
18. MAY RS: *Stochastic Aperture Techniques in Gamma-Ray Image Formation*, Ph.D. Thesis, University of Michigan, 1974
19. MAY RS, AKCASU AZ, KNOLL GF: γ -ray imaging with stochastic apertures. *Appl Optics* 13: 2589-2601, 1974
20. KORAL KF, ROGERS WL, BEIERWALTES WH: Gamma-ray imaging with a time-modulated pseudorandom aperture and an Anger camera. *J Nucl Med* 15: 508, 1974
21. HOSSFELD F, AMADORI R: *On Pseudorandom and Markov Sequences Optimizing Correlation Time-of-Flight Spectrometry*. Kernforschungsanlage Julich Report, Jul-684-FF, 1970
22. WILHELMI G: *Datenverarbeitungszentrale. Eine Übersicht über Differenzmengen mit Tabellen*. Kernforschungszentrum Karlsruhe Report KFK 1177, 1970